nature COMMUNICATIONS

ARTICLE

https://doi.org/10.1038/s41467-021-25780-4 OPEN

Multiband charge density wave exposed in a transition metal dichalcogenide

Árpád Pásztor[1✉], Alessandro Scarfato[1], Marcello Spera[1], Felix Flicker[2,3,4], Céline Barreteau[1], Enrico Giannini[1], Jasper van Wezel[5] & Christoph Renner[1✉]

In the presence of multiple bands, well-known electronic instabilities may acquire new complexity. While multiband superconductivity is the subject of extensive studies, the possibility of multiband charge density waves (CDWs) has been largely ignored so far. Here, combining energy dependent scanning tunnelling microscopy (STM) topography with a simple model of the charge modulations and a self-consistent calculation of the CDW gap, we find evidence for a multiband CDW in 2H-$NbSe_2$. This CDW not only involves the opening of a gap on the inner band around the K-point, but also on the outer band. This leads to spatially out-of-phase charge modulations from electrons on these two bands, which we detect through a characteristic energy dependence of the CDW contrast in STM images.

[1] Department of Quantum Matter Physics, Université de Genève, 24 quai Ernest Ansermet, CH-1211 Geneva 4, Switzerland. [2] Department of Physics, Clarendon Laboratory, Rudolph Peierls Centre for Theoretical Physics, University of Oxford, Parks Road, Oxford OX1 3PU, UK. [3] School of Physics and Astronomy, Cardiff University, Cardiff CF24 3AA, UK. [4] School of Mathematics, University of Bristol, Bristol BS8 1TW, UK. [5] Institute for Theoretical Physics Amsterdam and Delta Institute for Theoretical Physics, University of Amsterdam, Science Park 904, 1098XH Amsterdam, The Netherlands. ✉email: arpad.pasztor@unige.ch; christoph.renner@unige.ch

Imposing a new periodicity on a crystal leads to the reorganization of the electronic bands of the parent compound through their back-folding on the new Brillouin zone. New periodicities may be engineered in designer materials, for instance in artificial heterostructures with Moiré minigaps, or emerge due to a structural or electronic phase transition. The charge density wave state is an electronic order where the charge density develops a spatial modulation concomitantly to a periodic distortion of the atomic lattice and the opening of a gap in the quasi-particle spectrum. By reducing the electronic band energy, this gap compensates for the elastic and Coulomb energy costs associated with the formation of the CDW. It also lowers the degeneracy of the electronic states at the crossings of the folded bands. These are the points in the band structure of the parent compound that are connected by the wavevector of the new periodicity. Although a gap should open at all the crossings of the folded bands, previous studies only focused on the primary CDW gap around the Fermi-level, which leads to the highest energy gain of the reconstructed system. The existence of secondary gaps and associated charge modulations (CMs) remains largely unexplored.

In many cases, only a tiny fraction of the electrons are involved in the CDW formation. Therefore, the CDW gap manifests only as a slight reduction of the density of states (DOS)—which can depend on momentum—rather than a full depletion of the DOS. This makes it challenging to measure the CDW gap using spectroscopic probes such as angle-resolved photoemission spectroscopy (ARPES) and scanning tunnelling spectroscopy. This is particularly true for 2H-$NbSe_2$[1–5] (hereinafter simply $NbSe_2$). However, the effect of the redistributed electrons can be readily detected in topographic STM images, even for minute changes brought upon by the opening of the CDW gap as demonstrated in the following.

$NbSe_2$ is an iconic material of correlated electron physics. It hosts a nearly commensurate charge density wave below $T_{CDW} = 33.5$ K and a superconducting (SC) order below $T_{SC} = 7.2$ K[6–10]. $NbSe_2$ is a layered material with a three-fold symmetric crystal structure around the direction perpendicular to the layers (Fig. 1a). Each unit cell is composed of two slabs of Se–Nb–Se trilayers, where the Se lattices are 60° rotated, while the Nb atoms are aligned on top of each other in a trigonal prismatic coordination with the Se atoms.

The Fermi surface (FS) of $NbSe_2$ is mainly determined by the bonding and antibonding combinations of the Nb-4*d* orbitals[11,12] leading to double-walled barrel-shaped pockets around the K and Γ points of the hexagonal Brillouin-zone[2,3,13,14] (Fig. 1b). The charge-ordered state consists of three CDWs, which form along the three equivalent Γ*M* directions with wavevectors $(1-\delta)\frac{2}{3}|\Gamma M|$, where $\delta \approx 0.02$ and depends on temperature[10]. In real space, this yields a locally commensurate $3a_0 \times 3a_0$ superstructure delimited by discommensurations[15,16], where a_0 is the atomic periodicity.

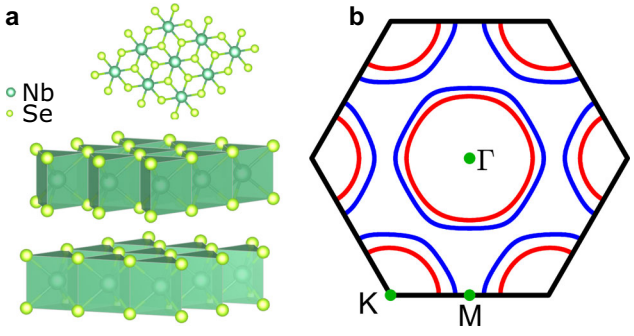

Fig. 1 Crystal structure and Fermi surface of $NbSe_2$. a The three-fold symmetric crystal structure from top and side views[33]. **b** The Fermi surface has been calculated using a two-band tight-binding fit to ARPES data[3]. Inner pockets (red) around Γ and *K* derive from one band, while the outer pockets (blue) derive from the second band; a small pancake-shaped pocket around Γ originating mainly from Se orbitals has been omitted.

The $3a_0 \times 3a_0$ reconstruction is readily accessible to topographic STM imaging. Its bias-dependent contrast has been the focus of previous studies, with particular emphasis on the contrast inversion expected in a classic Peierls scenario between images acquired above and below the CDW gap[17,18], and on the role of defects in stabilizing the CDW[5]. Sacks et al.[18] calculate the bias dependence of the CDW phase in a perturbative approach, considering a single band normal state description of $NbSe_2$. They find that the phase-shift of the CDW component of the local DOS can be very different from the 180° expected in a one-dimensional (1D) case (Supplementary Note VII) when changing the imaging bias across the Fermi level (E_F). However, their model does not reproduce the full bias dependence of the CDW amplitude and phase that we find.

Results and discussion

Bias dependent STM topography, CDW phase and amplitude. In Fig. 2a–c, we present a selection from numerous topographic STM images of the same region on a cleaved $NbSe_2$ surface at different sample biases (V_b) between −0.5 V and 0.5 V. They show a triangular atomic lattice with a superimposed $3a_0 \times 3a_0$ CDW modulation (see also Supplementary Fig. 1a), consistent with previous STM studies of unstrained bulk $NbSe_2$[4,5,16,17,19–22]. A defect-free region with a well resolved CDW outlined in red is magnified in Fig. 2d, f, h for each V_b. In order to identify the origin of the bias dependence of the topographic contrast in these images, we separate the atomic lattice and CDW contributions using Fourier filtering (Supplementary Note I). This analysis shows that the bias-dependent STM contrast is due to the changing CDW signal (Fig. 2e, g, i) since the corresponding atomic lattice contrast remains unchanged (see Supplementary Fig. 1).

The observed CDW pattern can be modelled as the sum of three plane waves as described in ref [16]. While each plane wave has its own phase $\varphi_i(\mathbf{r})$, which depends on a selected reference point, the *dephasing parameter* $\Theta(\mathbf{r}) = \varphi_1(\mathbf{r}) + \varphi_2(\mathbf{r}) + \varphi_3(\mathbf{r})$ mod 360° is uniquely defined for each particular CDW pattern, independent of any reference point. $\Theta(\mathbf{r})$ represents the internal CDW structure, quantifying the local relative position of the wavefronts of the three CDWs. In Fig. 2j–l, we show $\Theta(\mathbf{r})$ corresponding to the STM images in Fig. 2a–c, respectively. They were obtained by fitting the CDW contrast following the method described in ref. [16].

Each bias voltage is characterized by a dominant dephasing parameter (Fig. 2j–l), except in the vicinity of defects discussed later. This visual assessment is confirmed by the peaked histograms of $\Theta(\mathbf{r})$ (Supplementary Fig. 2). Fitting a Gaussian to these histograms allows to extract a well-defined dephasing parameter $\Theta_0(V_b)$ for each imaging bias (Supplementary Fig. 3). For a quantitative analysis of the bias dependence of Θ_0, we note that a given local CDW structure is represented by any arbitrary combination of $\varphi_i(\mathbf{r})$ summing up to the same dephasing parameter, in particular the one where all three phases are equal. Moreover, the threefold symmetry of the system implies there is no privileged plane wave among the three used to describe the CDW. These observations allow us to map the problem to a one-dimensional (1D) description with an apparent CDW phase $\varphi_0(V_b) = \Theta_0(V_b)/3$ (Supplementary Note III), and model $\varphi_0(V_b)$ to understand the bias dependent CDW pattern.

Plotting $\varphi_0(V_b)$ in Fig. 3a reveals a striking non-monotonic bias dependence, with an inflexion point around −0.15 V and a minimum slightly above the Fermi-level ($E_F = 0$ V). This dependence is robust as long as $\varphi_0(V_b)$ is extracted from

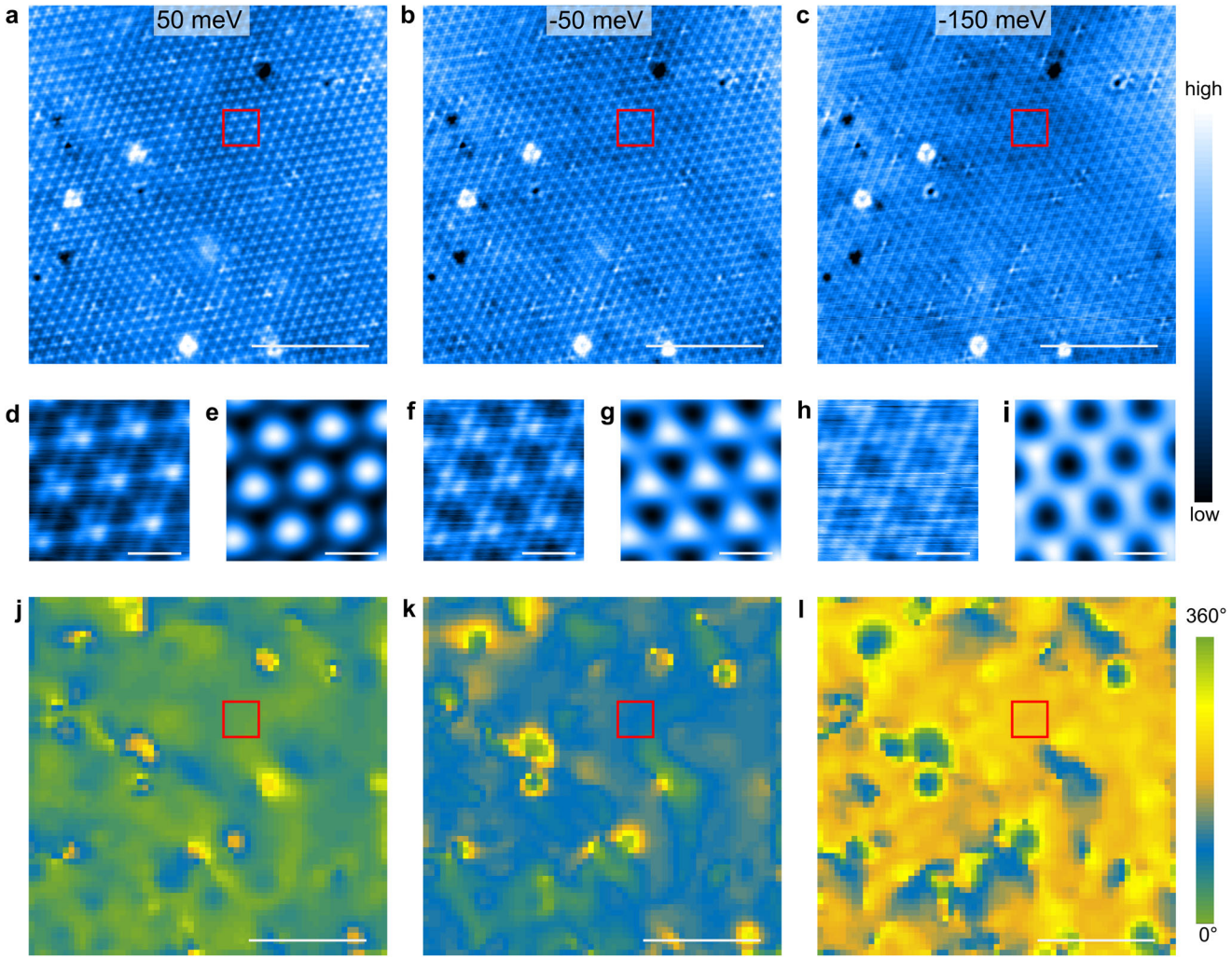

Fig. 2 Bias-dependent STM imaging of $NbSe_2$ at 1.2 K. Constant current topography showing the atomic lattice and CDW at **a** $V_b = 50$ mV, **b** $V_b = -50$ mV and **c** $V_b = -150$ mV (Solely for visualization, the STM image in **c** has been corrected for diagonal running sharp lines (with wavelength much longer than those of the CDW) which arose due to a tiny horizontal tilt of the sample leading to a least significant bit issue in the digital-analogue conversion of the piezo voltage.) with $I_t = 100$ pA. **d**, **f** and **h** are magnified images of the areas marked by the red squares in **a**, **b** and **c**, respectively. The overall imaging contrast is very different in these cases, although the atomic lattice appears identical in all images (Supplementary Fig. 1). **e**, **g** and **i** shows the magnified image of the large Fourier-filtered image of the CDWs at the same location as shown in **d**, **f** and **h**, respectively. It demonstrates that the variation of contrast observed in **d**, **f** and **h** is stemming from a variation in the appearance of the CDW at different biases. These appearances can be quantified by a single parameter: the dephasing parameter which describes the relative position of the three CDWs. **j**–**l** show the spatial variation of the dephasing parameter determined by fitting the CDW modulations of the STM images shown in **a**–**c**, respectively. The red squares correspond to the same area that is highlighted in **a**–**c** and magnified in **d**–**i**. Scalebars: 10 nm in **a**–**c** and **j**–**l**; 1 nm in **d**–**i**.

topographic STM images away from defects (Supplementary Fig. 4). Close to defects, the dephasing parameter $\Theta_0(V_b)$ is different and tends to depend much less on imaging bias (Supplementary Fig. 5). This is consistent with earlier findings that defects (and impurities) can act as strong pinning centres[23,24] locking the local phase of the CDW or driving the formation of CDW domains[25,26].

The CDW amplitude can be extracted in a similar way to the phase, by fitting the histogram of the local amplitudes $a_i(\mathbf{r})$ of each plane wave measured over the entire field of view with a Gaussian, and extracting the peak value $a_i(V_b)$. The bias dependence and magnitude of $a_i(V_b)$ is nearly the same for all three CDWs (Supplementary Fig. 6b). For the analysis, we consider the average of these three amplitudes at each bias $A_0(V_b) = (a_1(V_b) + a_2(V_b) + a_3(V_b))/3$ plotted in Fig. 3b.

Modelling and calculations. To understand the bias dependence of the CDW amplitude and phase in Fig. 3, we simulate topographic STM traces using a 1D model system (Supplementary Note VIII). In the simplest configuration corresponding to the Peierls reconstruction, we consider the contribution to the tunneling current of a single CM and its associated gap centred on E_F (Fig. 4a–c). In this case, traces at the same polarity are always in phase, whereas traces at opposite polarities always show contrast inversion (or a 180° phase shift in the present harmonic model). The latter, often considered as an identifying hallmark of the CDW state[27], clearly does not reproduce the data in Fig. 3a.

A single CM can only produce two sets of STM traces differing by contrast inversion in the vicinity of the gap. To generate a more complex bias dependence of the phase, we consider the possibility of a second CM whose associated gap opens in another band and away from E_F (Fig. 4d–f). If these two harmonic CMs are in phase (Fig. 4d), the resulting STM traces are either in-phase or 180° out of phase (Fig. 4e), unable to reproduce the data in Fig. 3a. To generate more structures in the bias dependence of the phase, we need to introduce a phase shift between the two CMs

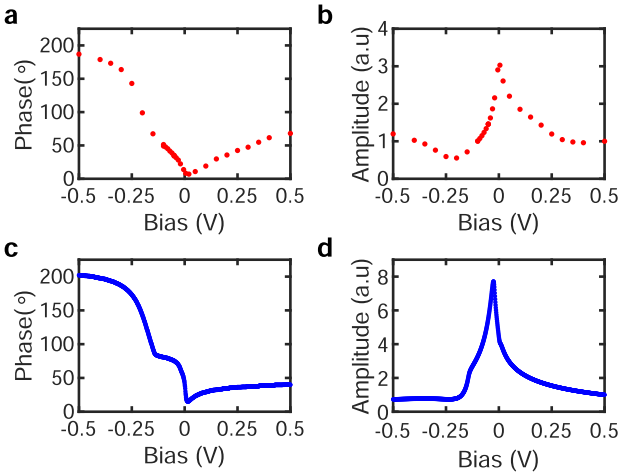

Fig. 3 Bias dependence of the phase and amplitude in experiments and in modelling. a and **b** show the bias dependence of the phase and amplitude of one of the unidirectional CDW extracted from the dephasing parameter and amplitude maps. **c** and **d** The phase and amplitude of the best matching simulations in the two-gap model. The data in **b** and **d** are normalized to their $V_b = 0.5$ V value.

(Figs. 4g–i). This leads to a phase that is no longer bi-modal, limited to two values differing by 180° as in Fig. 4c, f. It takes many different values (Fig. 4i), where the precise bias dependence is defined by the magnitude of the two gaps, their position relative to E_F and by the relative phase shift between the two CMs. The simulated STM topographic traces in Figs. 4b, e and h also reveal a pronounced bias-dependent imaging amplitude with distinct line-shapes in the three model cases discussed above (Supplementary Fig. 7).

The broad parameter space of our 1D model makes it challenging to run a self-converging fit to the data. Visually optimizing the size and position of the two gaps in Fig. 4i, we find a range of parameters (Supplementary Note X) simultaneously reproducing the experimental bias dependent CDW phase and amplitude data remarkably well (Fig. 3). As for the relative phase between the two CMs, it is chosen to minimize the Coulomb interaction of the CMs and to conform with the strong commensuration energy that locally locks them to the lattice. Reducing the Coulomb energy is obtained by introducing a phase shift between the two CMs, which can only be ±120° (Fig. 4g) to satisfy the lock-in criterion with the lattice given the $3a_0$ periodicity of the CDW.

In the following, we turn to theoretically modelling multiple CDW gaps on different bands in $NbSe_2$. We deploy self-

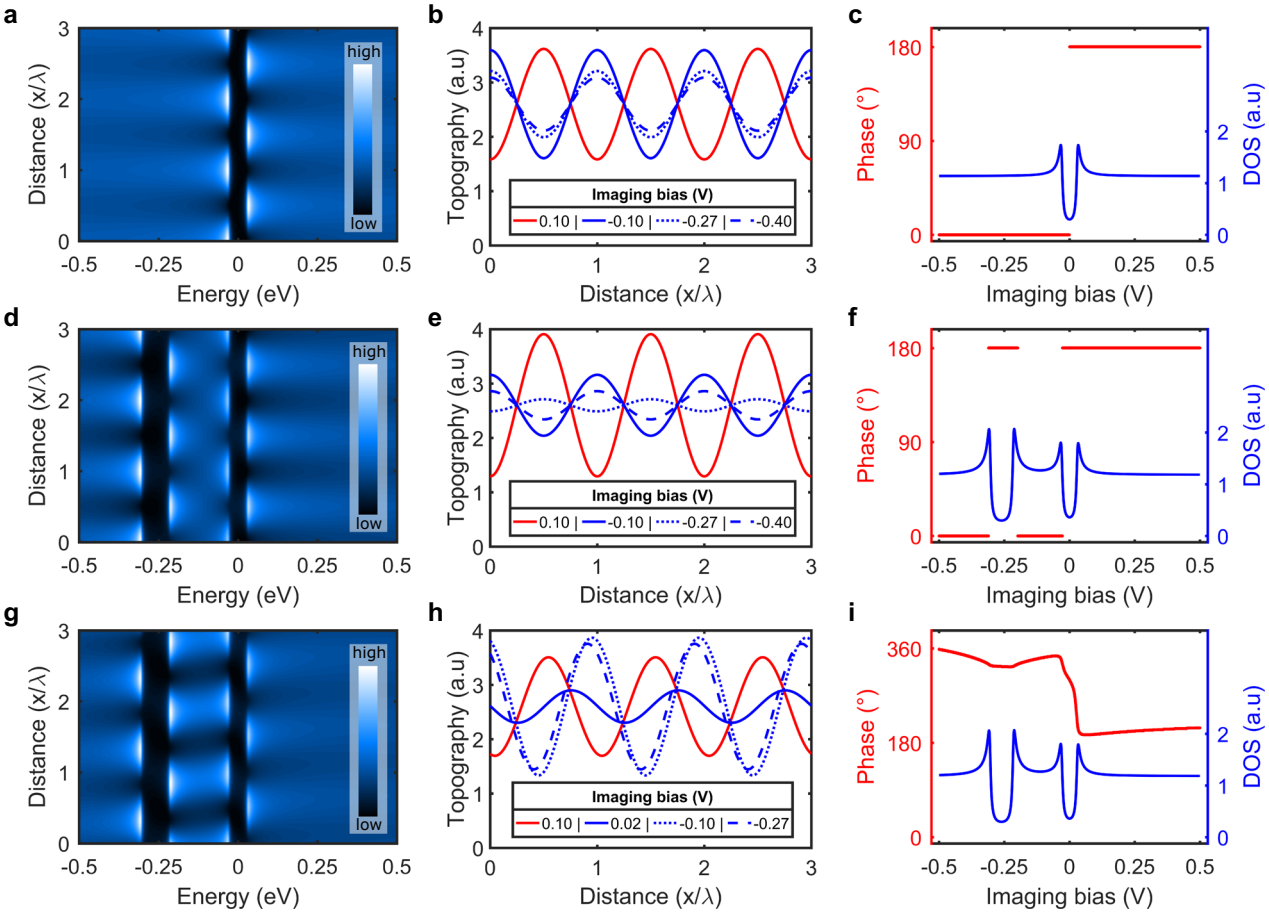

Fig. 4 One-dimensional model description of the bias-dependent phase of the CDW. a–c There is a single CM and the corresponding gap is centred at the Fermi level. **d–f** There are two CMs with two gaps that are centred at different energies (one at the Fermi-level and one below). There is no real-space phase difference between the CMs. **g–i** The same as **d–f** except that there is a 120° ($2\pi/3$) phase difference -one atom shift- between the two CMs. In all three cases, the first column shows the spatial and energy-dependent CDW local DOS maps. Second column: corresponding simulated topographic traces at selected biases (the actual bias value is shown in the legend). The red and blue topographic traces correspond to positive and negative sample biases, respectively. To clearly see the evolution of the phase and the amplitude the curves are offset vertically in **b**, **e** and **h** such that they all oscillate around the same value. Third column: bias dependence of the phase (left red axis) and DOS (spatially integrated local DOS from the first column, right blue axis).

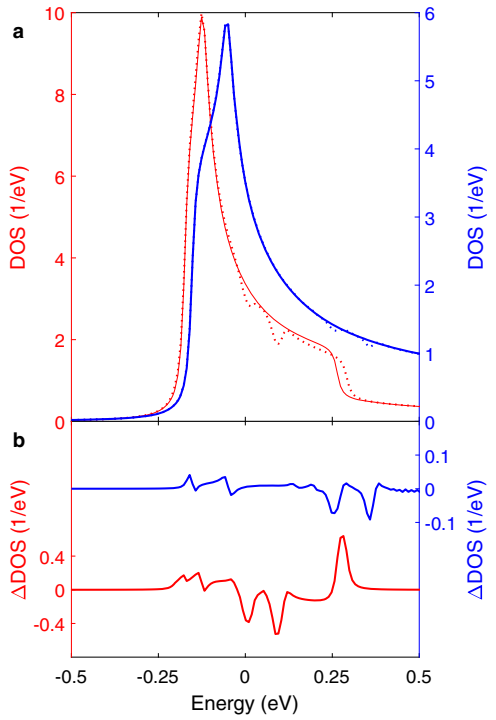

Fig. 5 Density of state of the two bands in the self-consistent calculations. a The red (blue) indicates the band making up the inner (outer) pockets; solid/dashed indicates the ungapped/gapped band structure, where gaps are included self-consistently at the mean-field level. **b** Difference between the gapped and ungapped cases in **a**, showing small DOS suppressions at energies away from E_F on both bands in addition to the gap at E_F on the inner band.

consistent calculations to include the CDW gap within the random phase approximation on the two-dimensional two-band tight-binding fit to the $NbSe_2$ band structure constrained by ARPES[3]. The corresponding FS shown in Fig. 1b consists of inner (red) and outer (blue) bands originating from symmetric and antisymmetric combinations of the Nb $d_{3z^2-r^2}$ orbitals. The model (see "Methods") was previously shown to accurately reproduce the full range of experimental measurements on the charge-ordered state[12,28]. The resulting DOS for the gapped and ungapped cases in each band are shown in Fig. 5a. To emphasize the DOS reduction accompanying the CDW phase transition, we plot the difference between the gapped and ungapped DOS for each band in Fig. 5b.

Our theoretical modelling shows a clear gap on the inner band at E_F, consistent with the gap measured by ARPES around the K-point[3]. Interestingly, Fig. 5b reveals further DOS reductions, for example near 100 meV on the inner band and −50 meV on the outer band. These features are indicative of CDW gaps opening away from E_F in addition to the (primary) gap at E_F, supporting the simple model we propose to understand the bias dependence of the CDW appearance in STM images of $NbSe_2$. According to Fig. 5b, there could even be more than two gaps. Consequently, we have included up to $n = 8$ gaps to our 1D model. However, the agreement with the data is similar for $n = 2$ and $n = 3$ (Supplementary Note XI), and we see no improvements adding more gaps.

In summary, the remarkable match between the bias dependence of the CDW contrast in STM topography and the simple 1D model proposed here provides compelling evidence that the CDW in $NbSe_2$ is composed of at least two out-of-phase CMs on the inner and outer bands. While a 180° phase shift between these two CMs would minimize the Coulomb energy, the complex bias dependence of the CDW amplitude and phase observed by STM can only be reproduced when considering also the commensuration energy. This highlights the importance of the coupling of charge order to the lattice, which manifests in the formation of discommensurations[15,16] and ultimately enables the observation of the multiband CMs uncovered here. The present study further highlights the power of topographic imaging to gain unique insight into detailed features of the CDW too faint to be detected accurately by tunneling spectroscopy. The formation of multiple modulations in response to new periodicities of a primary transition directly observed here, is extremely general and should in principle be present in all charge (and spin) density wave materials, and suggests new directions to explore in the physics of spatially modulated electronic orders.

Methods

Crystal growth and STM measurements. Single crystals of $NbSe_2$ were grown via iodine-assisted chemical vapour transport and cleaved in-situ at room temperature. STM experiments were done in UHV (base pressure below $2 \cdot 10^{-10}$ mbar) using tips mechanically cut from a PtIr wire and conditioned in-situ on a clean Ag(111) single crystal. The bias voltage was applied to the sample. STM images were recorded in constant current mode with at least 64 pixel/nm resolution. Details of the CDW amplitude and phase fitting procedure can be found in ref [16].

Self-consistent calculations. We carried out a 22-orbital Slater–Koster tight-binding fit[29] to the $NbSe_2$ band structure, constrained by ARPES measurements[2,3] and local density approximation numerical calculations[11]. This provided not only the band structure, but the orbital composition of the bands. We found that the two bands crossing the Fermi level are predominantly composed of the niobium $d_{3z^2-r^2}$ orbitals (>60% across the Brillouin zone). A third, small, pancake-shaped pocket centred on Γ derives primarily from the selenium p-orbitals and is therefore not expected to mix significantly with the other bands, in-keeping with experimental observations that it plays no role in the charge ordering. We then re-fit the two bands of interest using only the two relevant orbitals; the fit was indistinguishable from the phenomenological fit to ARPES data provided in ref. [3].

The Coulomb interaction can be neglected in $NbSe_2$, as the large DOSs at the Fermi level leads to strong screening. This remains true down to the lowest temperatures (above the SC transition at 7.2 K) since the CDW gap only opens on small regions of the FS. The relevant interaction is the electron-phonon coupling, for which we constructed an analytic expression following Ref. [30]. It has long been suggested that the CDW in $NbSe_2$ originates not from FS nesting, but from the dependence of the electron–phonon coupling on the momentum transfer in the phonon-mediated electron–electron scattering[11]. Our calculation includes the dependence of the coupling on the ingoing and outgoing electron momenta, as well as the orbital composition of the electronic bands scattered between. Only by taking all of these factors into account were we able to find a consistent explanation of the full range of experimental observations, including ARPES[2,3], scanning tunneling spectroscopy/microscopy[4], and inelastic X-ray scattering[31]. Our model has only one free parameter, the overall magnitude of the electron–phonon coupling, which we fixed using $T_{CDW} = 33.5$ K.

We modelled the effect of the CDW on the electronic band structure using the random phase approximation. We employed the Nambu–Gor'kov method to work within the gapped phase; this method consists of promoting the electronic Green's function to a 9×9 matrix, representing the tripling of the real-space unit cell in both lattice directions induced by the CDW formation. The CDW gap appears in off-diagonal elements, and diagonalisation then results in a gapped electronic band structure. We solved for the CDW gap self-consistently at high-symmetry points in the Brillouin zone, and used the results to constrain a tight-binding fit for the gap structure. We assumed the gap to be independent of energy. The CDW gap serves as an order parameter, and so our model naturally accounts for long-range CDW correlations. Further details of the method are given in refs. [12,28].

We found that a CDW gap opens at the Fermi level on the outer pocket centred on the K-point, along the MK line, in agreement with ARPES[2,3]. However, since the order parameter is non-zero at all points in the Brillouin zone, and at all energies, gaps also open wherever band crossings are introduced. This is the origin of the multiband CDW, evidenced by the suppression of DOS at energies below E_F seen in Fig. 5. We calculated the DOS at different energies, with and without the CDW gap, by summing over the Brillouin zone the spectral function found from the electronic Green's function.

Data availability

The data that support the findings of this study has been deposited in the Yareta repository (https://doi.org/10.26037/yareta:en553fvpkrdorgqtssxegl4tyi)[32].

Code availability

Computer codes are available upon reasonable request and preferably within a collaboration.

Received: 12 January 2021; Accepted: 1 September 2021;
Published online: 15 October 2021

References

1. Wang, C., Giambattista, B., Slough, C. G., Coleman, R. V. & Subramanian, M. A. Energy gaps measured by scanning tunneling microscopy. *Phys. Rev. B* **42**, 8890 (1990).
2. Borisenko, S. V. et al. Two energy gaps and fermi-surface "arcs" in $NbSe_2$. *Phys. Rev. Lett.* **102**, 166402 (2009).
3. Rahn, D. J. et al. Gaps and kinks in the electronic structure of the superconductor 2H-$NbSe_2$ from angle-resolved photoemission at 1 K. *Phys. Rev. B* **85**, 224532 (2012).
4. Soumyanarayanan, A. et al. Quantum phase transition from triangular to stripe charge order in $NbSe_2$. *Proc. Natl Acad. Sci. USA* **110**, 1623 (2013).
5. Arguello, C. J. et al. Visualizing the charge density wave transition in 2H-$NbSe_2$ in real space. *Phys. Rev. B* **89**, 235115 (2014).
6. Revolinsky, E., Spiering, G. A. & Beerntsen, D. J. Superconductivity in the niobium-selenium system. *J. Phys. Chem. Solids* **26**, 1029 (1965).
7. Wilson, J. A., DiSalvo, F. J. & Mahajan, S. Charge-density waves and superlattices in the metallic layered transition metal dichalcogenides. *Adv. Phys.* **24**, 117 (1975).
8. Harper, J. M. E., Geballe, T. H. & Di Salvo, F. J. Heat capacity of 2H-$NbSe_2$ at the charge density wave transition. *Phys. Lett. A* **54**, 27 (1975).
9. Long, J. R., Bowen, S. P. & Lewis, N. E. Anomalous resistivity of iodine-free 2H-$NbSe_2$. *Solid State Commun.* **22**, 363 (1977).
10. Moncton, D. E., Axe, J. D. & DiSalvo, F. J. Study of superlattice formation in 2H-$NbSe_2$ and 2H-$TaSe_2$ by neutron scattering. *Phys. Rev. Lett.* **34**, 734 (1975).
11. Johannes, M. D., Mazin, I. I. & Howells, C. A. Fermi-surface nesting and the origin of the charge-density wave in $NbSe_2$. *Phys. Rev. B* **73**, 205102 (2006).
12. Flicker, F. & van Wezel, J. Charge order from orbital-dependent coupling evidenced by $NbSe_2$. *Nat. Commun.* **6**, 7034 (2015).
13. Corcoran, R. et al. Quantum oscillations in the mixed state of the type II superconductor 2H-$NbSe_2$. *J. Phys.: Condens. Matter* **6**, 4479 (1994).
14. Rossnagel, K. et al. Fermi surface of 2H-$NbSe_2$ and its implications on the charge-density-wave mechanism. *Phys. Rev. B* **64**, 235119 (2001).
15. McMillan, W. L. Theory of discommensurations and the commensurate-incommensurate charge-density-wave phase transition. *Phys. Rev. B* **14**, 1496 (1976).
16. Pásztor, Á. et al. Holographic imaging of the complex charge density wave order parameter. *Phys. Rev. Res.* **1**, 033114 (2019).
17. Mallet, P., Sacks, W., Roditchev, D., Défourneau, D. & Klein, J. Spatial and energy variation of the local density of states in the charge density wave phase of 2H-$NbSe_2$. *J. Vac. Sci., Technol. B: Microelectron. Nanometer Struct.* **14**, 1070 (1996).
18. Sacks, W., Roditchev, D. & Klein, J. Voltage-dependent STM image of a charge density wave. *Phys. Rev. B* **57**, 13118 (1998).
19. Gao, S. et al. Atomic-scale strain manipulation of a charge density wave. *Proc. Natl Acad. Sci. USA* **115**, 6986 (2018).
20. Martinez-Castro, J. et al. Scanning tunneling microscopy of an air sensitive dichalcogenide through an encapsulating layer. *Nano Lett.* **18**, 6696 (2018).
21. Gye, G., Oh, E. & Yeom, H. W. Topological landscape of competing charge density waves in 2H-$NbSe_2$. *Phys. Rev. Lett.* **122**, 016403 (2019).
22. Guster, B. et al. Coexistence of elastic modulations in the charge density wave state of 2H-NbSe2. *Nano Lett.* **19**, 3027 (2019).
23. Fukuyama, H. Pinning in Peierls-Fröhlich state and conductivity. *J. Phys. Soc. Jpn.* **41**, 513 (1976).
24. Fukuyama, H. & Lee, P. A. Dynamics of the charge-density wave. I. Impurity pinning in a single chain. *Phys. Rev. B* **17**, 535 (1978).
25. Hildebrand, B. et al. Short-range phase coherence and origin of the 1T-$TiSe_2$ charge density wave. *Phys. Rev. B* **93**, 125140 (2016).
26. Novello, A. M. et al. Stripe and short range order in the charge density wave of 1T-Cu_x $TiSe_2$. *Phys. Rev. Lett.* **118**, 017002 (2017).
27. Spera, M. et al. Insight into the charge density wave gap from contrast inversion in topographic STM images. *Phys. Rev. Lett.* **125**, 267603 (2020).
28. Flicker, F. & van Wezel, J. Charge order in $NbSe_2$. *Phys. Rev. B* **94**, 235135 (2016).
29. Slater, J. C. & Koster, G. F. Simplified LCAO method for the periodic potential problem. *Phys. Rev.* **94**, 1498 (1954).
30. Varma, C. M., Blount, E. I., Vashishta, P. & Weber, W. Electron-phonon interactions in transition metals. *Phys. Rev. B* **19**, 6130 (1979).
31. Weber, F. et al. Optical phonons and the soft mode in 2H-$NbSe_2$. *Phys. Rev. B* **87**, 245111 (2013).
32. Pásztor, Á. et al. Dataset Multiband charge density wave exposed in a transition metal dichalcogenide. https://doi.org/10.26037/yareta:en553fvpkrdorgqtssxegl4tyi (2021).
33. Momma, K. & Izumi, F. Vesta 3 for three-dimensional visualization of crystal, volumetric and morphology data. *J. Appl. Crystallogr.* **44**, 1272 (2011).

Acknowledgements

We acknowledge A. F. Morpurgo and I. Maggio-Aprile for inspiring discussions. We thank A. Guipet and G. Manfrini for their technical support in the STM laboratories. This project was supported by Div.2 (Grant No. 182652) and Sinergia (Grant No. 147607) of the Swiss National Science Foundation. F. F. acknowledges support from the Astor Junior Research Fellowship of New College, Oxford.

Author contributions

C.R. designed the experiment. M.S. and A.S. took care of the STM experiments. Á.P. performed the data analysis. F.F. and J.v.W. performed the self-consistent calculations. Á.P. did the one-dimensional model simulations. C.B. and E.G. synthesized the bulk crystals. Á.P., A.S., F.F., J.v.W. and C.R. wrote the paper. All authors contributed to the scientific discussions and manuscript revisions.

Competing interests

The authors declare no competing interests.

Additional information

Supplementary information The online version contains supplementary material available at https://doi.org/10.1038/s41467-021-25780-4.

Correspondence and requests for materials should be addressed to Árpád Pásztor or Christoph Renner.

Peer review information *Nature Communications* thanks the anonymous reviewers for their contribution to the peer review of this work. This article has been peer reviewed as part of Springer Nature's Guided Open Access initiative.

Reprints and permission information is available at http://www.nature.com/reprints

Publisher's note Springer Nature remains neutral with regard to jurisdictional claims in published maps and institutional affiliations.

Supplementary Information for Multiband charge density wave exposed in a transition metal dichalcogenide

Árpád Pásztor,[1,*] Alessandro Scarfato,[1] Marcello Spera,[1] Felix Flicker,[2,3,4] Céline Barreteau,[1] Enrico Giannini,[1] Jasper van Wezel,[5] and Christoph Renner[1,†]

[1] *Department of Quantum Matter Physics, Université de Genève, 24 quai Ernest Ansermet, CH-1211 Geneva 4, Switzerland.*

[2] *Rudolph Peierls Centre for Theoretical Physics, University of Oxford, Department of Physics, Clarendon Laboratory, Parks Road, Oxford OX1 3PU, United Kingdom*

[3] *School of Physics and Astronomy, Cardiff University, Cardiff CF24 3AA, United Kingdom*

[4] *School of Mathematics, University of Bristol, Bristol BS8 1TW, United Kingdom*

[5] *Institute for Theoretical Physics Amsterdam and Delta Institute for Theoretical Physics, University of Amsterdam, Science Park 904, 1098 XH Amsterdam, The Netherlands*

CONTENTS

* arpad.pasztor@unige.ch

† christoph.renner@unige.ch

I. FOURIER-FILTERING TO SEPARATE THE ATOMIC LATTICE AND CDW CONTRIBUTIONS TO THE STM TOPOGRAPHY.

We use Fourier filtering to separate the atomic lattice and CDW signals in topographic STM images. We start with the Fourier transform (FT) of the STM image, e.g. Fig. 2a of the main text. This yields a sharp and intense peak structure at the first order Bragg-peaks of the CDW and atomic modulations outlined in Suppl. Fig. 1a with red and blue circles, respectively. To obtain the image corresponding to the atomic (CDW) lattice, we mask the atomic (CDW) component by suppressing the values outside the blue (red) circles in the FT and we take the inverse transform of this modified map. These operation are always performed on the large scale STM images (Figs. 2a, b and c).

Suppl. Figs. 1b-d show magnified regions of the Fourier filtered STM images in Figs. 2a-c. They reveal the atomic lattice at the exact same locations as the CDW contributions shown in Figs. 2e, g and i, respectively. The atomic lattice contribution is the same in all three images, supporting the conclusion that the contrast changes in Figs. 2d, f and h are primarily due to changes in the CDW contrast with bias.

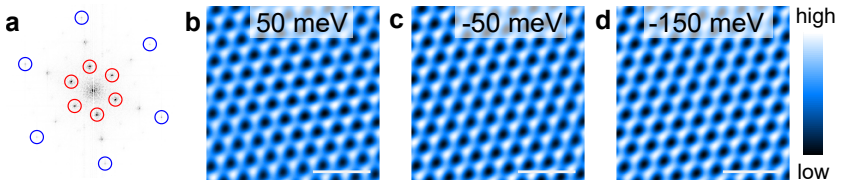

Suppl. Fig. 1. **Atomic lattice contribution to the STM topography.** **a** Fourier-transform of the STM image shown in Fig. 2a of the main text. The blue and red circles mark the peaks corresponding to the atomic and CDW components, respectively. Magnified Fourier filtered images of the atomic lattice at **b** $V_b = 50$ mV, **c** $V_b = -50$ mV and **d** $V_b = -150$ mV corresponding to the exact same region as shown in Figs. 2d-i of the main text. Scalebar: 1 nm.

II. HISTOGRAMS OF THE DEPHASING PARAMETER

Suppl. Figs. 2a, b, and c show the histograms of the dephasing parameter maps $\Theta(\mathbf{r})$ shown in Figs. 2j, k, and l in the main text, respectively. They all exhibit a well defined peak, which we fit with a Gaussian to determine the most frequent dephasing parameter

$\Theta_0(V_b)$ for each imaging bias.

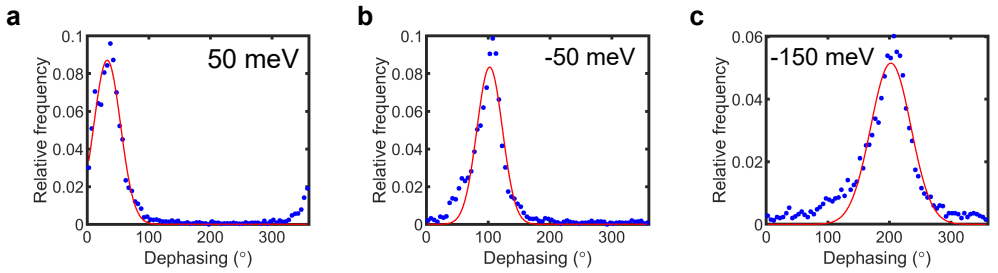

Suppl. Fig. 2. **Histograms of the dephasing parameter maps. a**, **b**, and **c** corresponds to the $\Theta(\mathbf{r})$ maps shown in Figs. 2j, k, and l in the main text, respectively. The solid red lines show the Gaussian fit of the dominant peak in each histogram. The peak position defines the representative dephasing parameter $\Theta_0(V_b)$ for each imaging bias V_b.

III. MAPPING THE DEPHASING PARAMETER TO THE PHASE OF A UNIDIRECTIONAL CDW

The appearance of the CDW pattern observed by STM can be reproduced by the sum of three plane waves [1]. The dephasing parameter $\Theta(\mathbf{r}) = \varphi_1(\mathbf{r}) + \varphi_2(\mathbf{r}) + \varphi_3(\mathbf{r})$ mod 360°, where $\varphi_i(\mathbf{r})$ is the phase of each plane wave, is a unique representation of a given CDW pattern. Any arbitrary combination of $\varphi_i(\mathbf{r})$, $i = (1, 2, 3)$, summing up to the same dephasing parameter, will describe this CDW pattern. In particular the combination where all three phases are equal. Based on the threefold symmetry of the system, there is no preferred direction and one may further assume that all three follow the same bias dependence.

These observations allow us to map $\Theta(\mathbf{r})$ to a one-dimensional problem we can more easily model. We start from $\Theta_0(V_b)$ (Suppl. Fig. 3a) obtained for each bias as shown in Suppl. Fig. 2. Next, we remove any phase jumps due to the 360° periodicity of $\Theta_0(V_b)$ (Suppl. Fig. 3b). Finally, we divide the resulting phase by three to obtain a representative one-dimensional (1D) phase $\varphi_0(V_b) = \Theta_0(V_b)/3$ (Suppl. Fig. 3c). Note that since the dephasing parameter $\Theta_0(V_b)$ is 360° periodic, we can freely add an integer times 120° to $\varphi_0(V_b)$ and still get the same dephasing parameter.

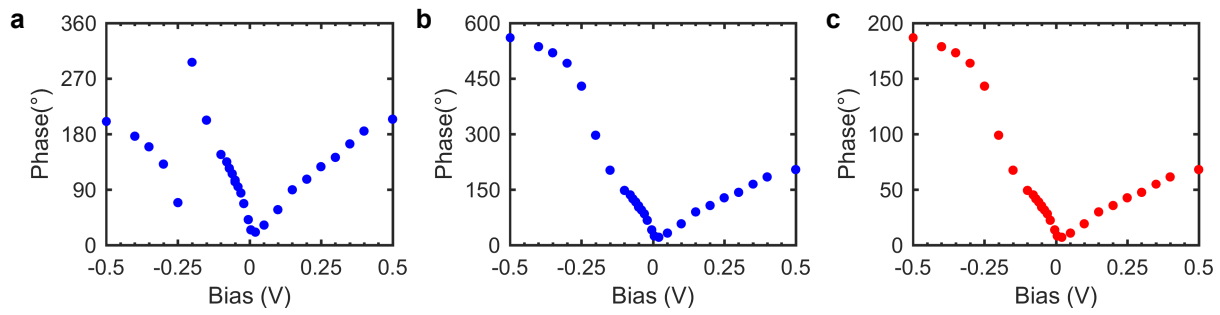

Suppl. Fig. 3. **Mapping the dephasing parameter to the phase of a unidirectional CDW.** **a** Dephasing parameter $\Theta_0(V_b)$ mod 360° as obtained from the local fitting of the real space charge modulation. The jump at -0.2 V is due to the 360° periodicity. **b** To remove the jump at -0.2 V, we add 360° to $\Theta_0(V_b)$ for V_b <-0.2 V (extended zone scheme). **c** $\varphi_0(V_b) = \Theta_0(V_b)/3$ mapping the extended zone dephasing parameter to the phase of a unidirectional CDW.

IV. BIAS DEPENDENCE OF THE PHASE AWAY FROM DEFECTS

Here we demonstrate that the scheme to extract the bias dependent phase from topographic STM images is robust. The analysis in the main text is based on the phase extracted from the entire field of view (FOV) of Figs. 2a, b and c. This FOV combines regions away from defects with different topographic patterns. Here we demonstrate that although each region may correspond to a slightly different phase value, the bias dependence of the phase remains the same.

In Suppl. Fig. 4a, we highlight eight regions from which we extract the CDW phase as a function of bias plotted in Suppl. Fig. 4b. The inset of panel b shows the same data offset for clarity. For the small regions (1-4), there are not enough points for a reasonable histogram. Therefore, we use a spatial average for the dephasing parameter in these regions. In the large regions, we extract the phase as described in the main text: we fit a Gaussian to the histogram of the dephasing parameter $\Theta(\mathbf{r})$ to determine the most frequent one $\Theta_0(V_b)$. We are aware that in general the most frequent value and the average may not coincide, but this was not a problem for the areas with homogeneous $\Theta(\mathbf{r})$ selected here.

Independently of the size or the precise location of the defect-free area from which we extract the phase, we always find the same bias dependence within a small spread. This is most remarkable when comparing regions that appear differently in the STM image,

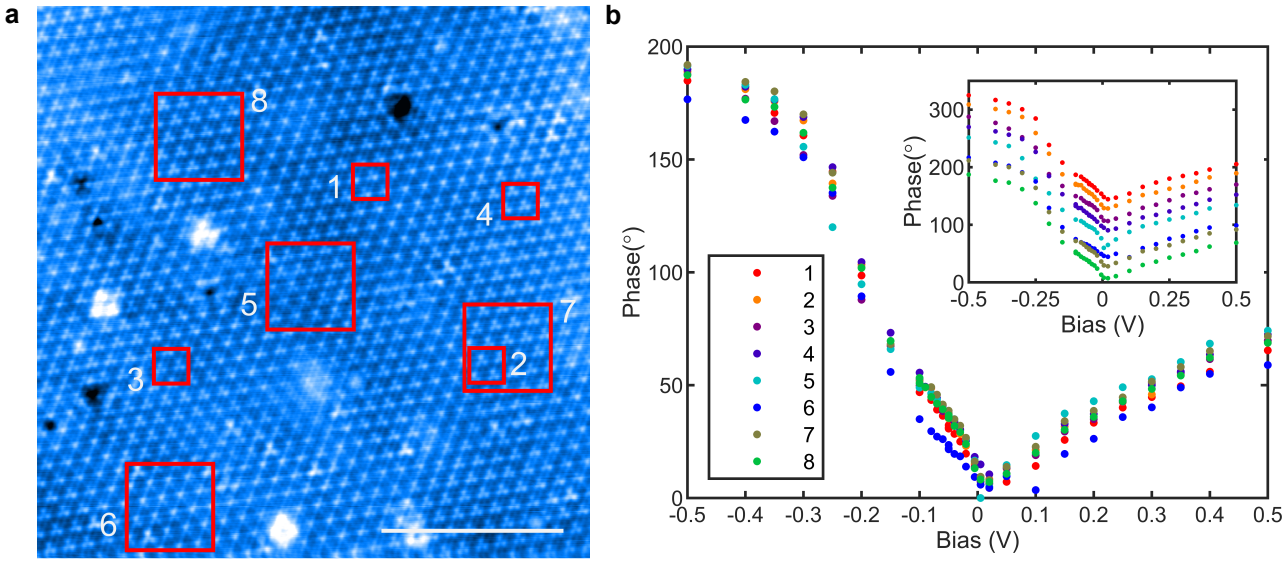

Suppl. Fig. 4. **Phase extracted away from defects. a** The same STM image as in Fig. 2a with numbered red squares marking the different areas where we extract the phase. Scalebar: 10 nm. **b** STM imaging bias dependence of the phase extracted at the marked regions. Inset: the same curves with a vertical offsets for clarity.

e.g regions 1 and 4 or regions 6 and 7. As the dephasing parameter only accounts for the appearance of the CDW pattern alone and not for its registry to the atomic lattice, the above observations imply that the CDW is composed of areas (connected by discommensuration with rapidly varying phase [1, 2]) where the CDW pattern is laterally shifted with respect to the atomic lattice. This is consistent with recent studies finding CDW domains with identical internal structures but with a distinct registry to the atomic lattice [3, 4].

V. BIAS DEPENDENCE OF THE CDW PHASE IN THE VICINITY OF DEFECTS

The impact of defects and impurities on the CDW is the focus of numerous studies, and is beyond the scope of the present investigation. Defects can act as strong pinning centers [5, 6], locking the local CDW to a particular phase or breaking it up into phase domains [7, 8]. In line with these studies, our analysis shows a very different behaviour of the CDW phase in the vicinity of defects, with a different and often weaker dependence on the imaging bias. This is illustrated in Suppl. Fig. 5 for a selection of defects. Similar looking defects in

the topography (Suppl. Fig. 5a) can drive a similar bias dependence of the CDW phase in their vicinity (defects 2 and 4), but also very different ones (e.g. defects 1 and 3, or 6 and 7). The latter may reflect de-pinning and re-pinning of the CDW at a given defect site in response to the repeated scanning of the same area at different biases.

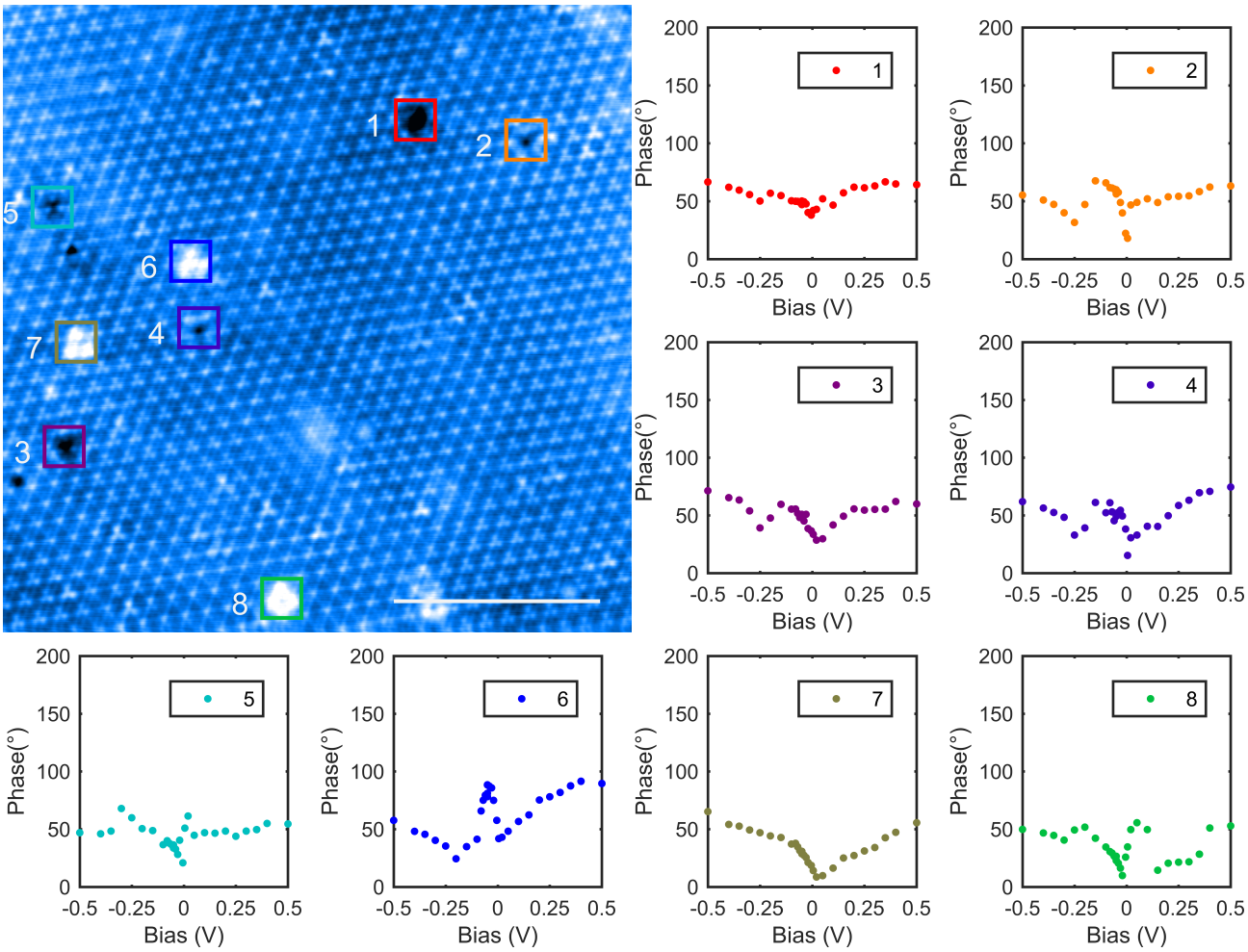

Suppl. Fig. 5. **Phase extracted around defects.** Main panel: the same STM image as in Fig. 2a with numbered coloured squares marking the different areas where we extract the phase. Scalebar: 10 nm. Small panels: the STM imaging bias dependence of the phase extracted at the marked regions.

Suppl. Fig. 5 graphically shows the importance of carefully considering defects in our analysis of the bias dependent CDW contrast. While the bias dependence varies a lot near different defects, it is consistently the same in the defect-free regions, independent of their location in the defect landscape (see Suppl. Fig. 4). This is a a very strong indication that

the defect-free regions we consider reveal intrinsic properties of the CDW modulation in $NbSe_2$. These regions are exempt of any local spectroscopic or topographic features at some specific bias that would be expected in presence of some hidden or subsurface defects. Moreover, the CDW Fourier peaks are sharp and well defined, unlike the characteristic signatures expected if defects were affecting the clean regions (see e.g. [9] and [10]). Finally, if strain due to the proximity to the visible defects or due to some hidden subsurface defects was affecting the clean regions we consider for our analysis, we would expect some anisotropy in the bias dependence of the CDW components (e.g. the stripes observed in [11]). This is not consistent with the perfectly homogeneous bias dependence of the three CDW component amplitudes depicted in Suppl. Fig. 6. All these experimental facts point to the same conclusion, that our multiband analysis is neither affected by proximity to the visible defects shown in Suppl. Fig. 5 nor by invisible subsurface defects.

VI. THE CDW IMAGING AMPLITUDE

In Suppl. Fig. 6a we show a map of the amplitude $a_1(\mathbf{r})$ obtained by fitting the CDW modulation along one of the three directions in Fig. 2a. The histogram of this amplitude map has a well defined peak, which we fit with a Gaussian to extract an amplitude $a_1(V_b)$ representative for the entire field-of-view for each imaging bias V_b. We repeat the same procedure for the other two directions to extract $a_2(V_b)$ and $a_3(V_b)$. All three a_i, (i=1,2,3), have a very similar bias dependence as seen in Suppl. Fig. 6b, prompting us to use their average at each bias in Fig 3b of the main text.

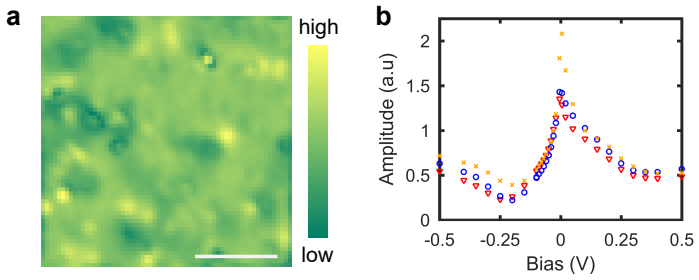

Suppl. Fig. 6. **The CDW imaging amplitude. a** Map of the local amplitude $a_1(\mathbf{r})$ of the CDW along one of the principle directions extracted from the STM image in Fig. 2b. Scalebar: 10 nm. **b** Bias dependence of the representative amplitudes a_i, (i=1,2,3) of each of the three one directional CDWs forming the CDW in Fig. 2.

VII. SPATIAL AND ENERGY DEPENDENCE OF THE LDOS IN A 1D CDW

In the following, we derive an expression of the energy and spatial dependence of the local density of states (DOS) in a 1D CDW. A similar derivation is presented in the supplementary material of ref. [12]. We start with the expressions from Grüner's book [13]:

$$\rho(x,k) = U_k^2 + V_k^2 - 2U_k V_k \cos(2k_F x + \varphi), \tag{1}$$

where $U_k^2 = \frac{1}{2}\left(1 - \frac{\epsilon_k}{E_k}\right)$ and $V_k^2 = \frac{1}{2}\left(1 + \frac{\epsilon_k}{E_k}\right)$. $\epsilon_k = \hbar v_F(k - k_F)$ is the normal state dispersion linearised around the Fermi-energy and $E_k = \mathrm{sgn}(\epsilon_k)\sqrt{\epsilon_k^2 + \Delta^2}$ is the dispersion in the CDW state, where Δ is the CDW energy gap. All energies are measured from the Fermi-energy. Inserting U_k and V_k into Supplementary Eq. 1 we get:

$$\begin{aligned}
\rho(x,k) =& 1 - \sqrt{1 - \frac{\epsilon_k^2}{E_k^2}}\cos(2k_F x + \varphi) = \\
=& 1 - \sqrt{\frac{E_k^2 - \epsilon_k^2}{E_k^2}}\cos(2k_F x + \varphi) = \\
=& 1 - \frac{\Delta}{E_k}\cos(2k_F x + \varphi).
\end{aligned} \tag{2}$$

We get the energy dependent local DOS from the following condition for the total number of states: $N = \int \rho(x,E)dE = \sum_k \rho(x,k) = \int_k \frac{L}{\pi}\rho(x,k)dk$ which yields:

$$
\begin{aligned}
\rho(x,E)dE =& \rho(x,k)\frac{L}{\pi}dk \\
\rho(x,E) =& \rho(x,k)\frac{L}{\pi}\frac{dk}{dE} = \rho(x,k)\frac{L}{\pi}\left(\frac{dE}{dk}\right)^{-1} \\
=& \rho(x,k)\frac{L}{\pi}\left(\mathrm{sgn}(\epsilon_k)\frac{\epsilon_k \hbar v_F}{\sqrt{\epsilon_k^2+\Delta^2}}\right)^{-1}
\end{aligned}
\tag{3}
$$

Finally, by omitting the index for k:

$$
\begin{aligned}
\rho(x,E) =& \mathrm{sgn}(E)\frac{1}{\hbar v_F}\frac{L}{\pi}\left(1-\frac{\Delta}{E}\cos(2k_F x+\varphi)\right)\left(\frac{\epsilon_k}{\sqrt{\epsilon_k^2+\Delta^2}}\right)^{-1} = \\
=& \left\{\text{using that } \epsilon_k^2 = E^2-\Delta^2 \text{ and that DOS at } \epsilon_F \text{ is } \mathcal{N}(E_F) = \frac{L}{\pi}\frac{1}{\hbar v_F}\right\} = \\
=& \mathrm{sgn}(E)\mathcal{N}(E_F)\left(1-\frac{\Delta}{E}\cos(2k_F x+\varphi)\right)\left(\frac{E}{\sqrt{E^2-\Delta^2}}\right)
\end{aligned}
\tag{4}
$$

VIII. CALCULATION OF THE CONSTANT CURRENT TOPOGRAPHY

We calculate 1D constant current topographic traces $z_0(x,V)$ by determining the tip-sample distance d at a given bias V and lateral position x that satisfies the constant current condition:

$$
I_{setpoint} - |I(d=z_0,x,V)| = 0, \tag{5}
$$

where $I_{setpoint} > 0$ is the set-point tunnelling current and $I(d,x,V)$ is the tunnelling current at a given tip-sample distance, lateral position and bias. To calculate the tunnelling current, we use the Bardeen equation for a 1D barrier in the limit of zero temperature [14]. First, we assume that the tip DOS does not depend on energy: $\rho_{tip}(E) = \rho_{tip}$. With this approximation, in the limit $T \to 0$, the tunnelling current is given by

$$
I(d,x,V) = \frac{4\pi e}{\hbar}\rho_{tip}\int_0^{eV}\rho_{sample}(x,E)\,|M(d,E,V)|^2\,dE, \tag{6}
$$

where $M(d, E, V)$ is the tunnelling matrix element and $\rho_{sample}(x, E)$ is the local DOS of the sample. For the matrix element we use the result obtained for the 1D barrier [14]:

$$M(d, E, V) = C_M \frac{\hbar^2}{m} \kappa e^{-\kappa d}, \tag{7}$$

where C_M is a constant and κ is determined by the average work function of the tip and sample ($\Phi_0 = (\Phi_{tip} + \Phi_{sample})/2$) as

$$\kappa(V, E) = \sqrt{\frac{2m}{\hbar^2}\left(\Phi_0 + \frac{eV}{2} - E\right)} \tag{8}$$

Grouping all the constants in C_I, the tunnelling current reads

$$I(d, x, V) = C_I \int_0^{eV} \rho_{sample}(x, E)\kappa^2(V, E)e^{-2\kappa(V,E)d} dE. \tag{9}$$

Note that the above formalism is valid only for finite V. At $V = 0$ there is no net tunnelling current and the measurement cannot be performed. Formally, in the $V \to 0$ limit, $I \to 0$ as the integration range goes to zero. To maintain a finite current, the tip sample distance must be reduced $d \to -\infty$, meaning that the tip crashes into the sample. Technically speaking, it is not possible to record constant current images at zero bias as there is no tunnelling current for any positive tip-sample distance. In the calculations we avoid this situation by never evaluating the current at strictly zero bias.

We model the density of states of the sample $\rho_{sample}(x, E)$ by the sum of three terms: $\rho_{sample}(x, E) = \rho_0 + \rho_1(x, E) + \rho_2(x, E)$. ρ_0 is a constant background while ρ_1 and ρ_2 are the DOS variations due to the two CMs:

$$\rho_1(x, E) = \Re\left(\mathrm{sgn}(E - \varepsilon_1)\left(1 - \frac{\Delta_1}{(E + i\Gamma - \varepsilon_1)}\cos(k_{CDW}x)\right)\frac{(E + i\Gamma - \varepsilon_1)}{\sqrt{(E + i\Gamma - \varepsilon_1)^2 - \Delta_1^2}}\right) \tag{10}$$

and

$$\rho_2(x,E) = \Re\left(\mathrm{sgn}(E-\varepsilon_2)\left(1-\frac{\Delta_2}{(E+i\Gamma-\varepsilon_2)}\cos(k_{CDW}x-\varphi)\right)\frac{(E+i\Gamma-\varepsilon_2)}{\sqrt{(E+i\Gamma-\varepsilon_2)^2-\Delta_2^2}}\right), \tag{11}$$

where $\Delta_{1,2}$ are the size of the gaps, $\varepsilon_{1,2}$ are the energies where the gaps are centred (gap midpoint) with respect to E_F, $k_{CDW} = 2\pi/\lambda_{CDW}$ is the CDW ordering vector, λ_{CDW} the wavelenght and φ a real-space phase difference between the two CMs. We used $\Gamma = 0.005$ eV for all the calculations presented in this work.

In order to calculate the constant current topographic traces, we solve numerically Supplementary Eq. 5 where we use Supplementary Eq. 9 for the tunnelling current and $\Phi_0 = 5.2$ eV for the average tip-sample work function (W and $NbSe_2$). To simulate a realistic situation we set C_I and ρ_0 such that the average tip-sample distance at a given bias (away from zero) is in the 5-8 Å range when the tunnelling current setpoint is 100 pA. The phase and amplitude at a given bias is simply determined from the position of the maximum and from the difference of the maximum and minimum value in the calculated constant current topographic traces.

IX. BIAS DEPENDENCE OF THE CDW AMPLITUDE IN THE DIFFERENT MODELS

In Suppl. Fig. 7, we present the bias dependence of the CDW amplitude calculated using the above method for the three models discussed in Fig. 4 of the main text.

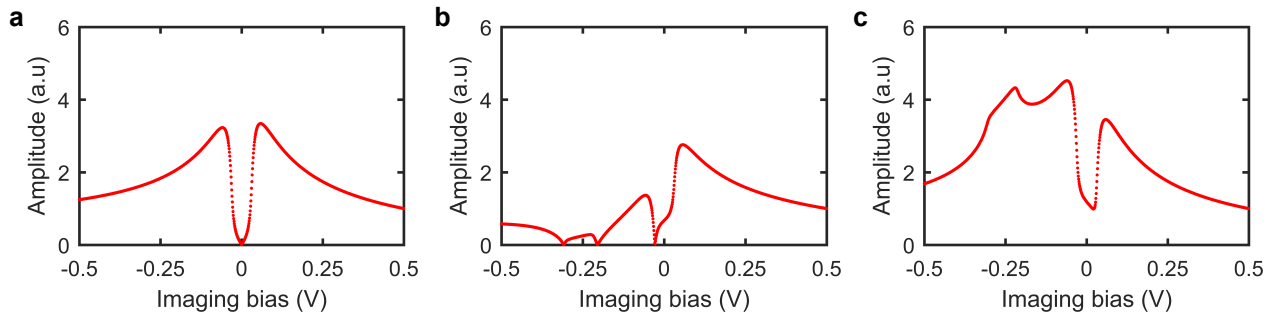

Suppl. Fig. 7. **Bias dependence of the amplitude of the CDW signal of the STM topography in the different 1D situation discussed in Fig 4. a** A single CM with a gap at the Fermi level. **b** Two CMs with the two gaps centred at different energies, but without any real-space phase difference between the CMs. **c** Same as **b**, but with a 120° ($2\pi/3$) phase difference between the CMs. For clarity, all the curves are normalized to their value at $V_b = 0.5$ V.

X. OPTIMIZED PARAMETERS OF THE TWO-GAP MODEL

To compare the two-gap model with our experimental data, we performed a visual optimization of the main parameters of the model: the size of the two gaps ($\Delta_{1,2}$) and their midgap position ($\varepsilon_{1,2}$). The model shows an excellent qualitative agreement with the experimental data (Fig. 3) for the following parameter ranges: $\Delta_1 \in [8, 16]$ meV, $\Delta_2 \in [45, 75]$ meV, $\varepsilon_1 \in [-14, -2]$ meV and $\varepsilon_2 \in [-100, -65]$ meV, where $\varepsilon_{1,2}$ are measured from E_F. With the parameters in these ranges the model reproduces the overall line-shape of the bias dependence of both the amplitude and the phase, and all the main features of the experimental data as discussed in the main text. In Figs. 3c and d we plot the bias dependence of the phase and amplitude obtained in the model using the parameters at the middle of the above ranges: $\Delta_1 = 12$ meV, $\Delta_2 = 60$ meV, $\varepsilon_1 = -8$ meV and $\varepsilon_2 = -82.5$ meV.

XI. PHASE AND AMPLITUDE IN THE THREE-GAP MODEL

We have also calculated the bias dependence of the phase and amplitude in a three-gap model by considering one more gap and a concomitant CM. The third CM we set in-phase with the second, i.e 120° out-of-phase to the first. In Suppl. Fig. 8 we use the same size and position of the gap ($\Delta_1 = 12$ meV and $\varepsilon_1 = -8$ meV) for the first CM as in the optimized two-gap model, and we split the second gap of the optimized two-gap model into two for the second and third CM of the three-gap model: $\Delta_2 = 30$ meV, and $\varepsilon_2 = -43$ meV, $\Delta_3 = 30$ meV, and $\varepsilon_3 = -123$ meV. The obtained bias dependence of the phase and amplitude of the CDW signal (Suppl. Figs. 8c and d) shows similarly good qualitative agreement with the experimental data (Suppl. Figs. 8a and b) as in the two-gap model (Fig. 3)

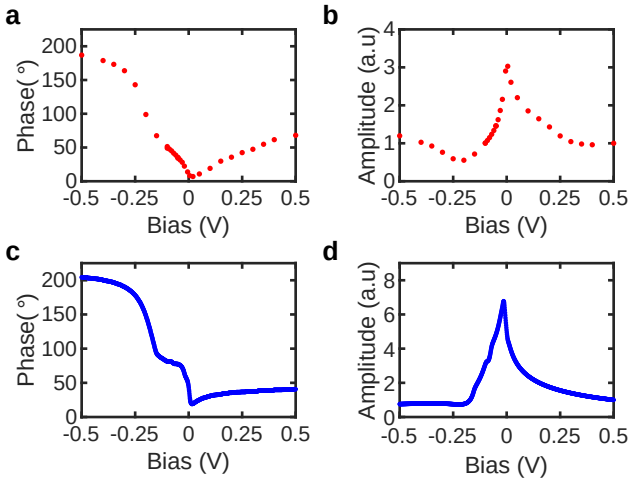

Suppl. Fig. 8. **Phase and amplitude in the three-gap model. a**, **b** Bias dependence of the phase and amplitude of the CDW signal in experiments (the same as in Fig. 3) and **c**, **d** in a three-gap model model. The data in **b** and **d** are normalized to their $V_b = 0.5$ V value.

[1] Á. Pásztor, A. Scarfato, M. Spera, C. Barreteau, E. Giannini, and C. Renner, Holographic imaging of the complex charge density wave order parameter, Physical Review Research **1**, 033114 (2019).

[2] W. L. McMillan, Theory of discommensurations and the commensurate-incommensurate charge-density-wave phase transition, Phys. Rev. B **14**, 1496 (1976).

[3] G. Gye, E. Oh, and H. W. Yeom, Topological landscape of competing charge density waves in 2H-$NbSe_2$, Physical Review Letters **122**, 016403 (2019).

[4] B. Guster, C. Rubio-Verdú, R. Robles, J. Zaldívar, P. Dreher, M. Pruneda, J. . Silva-Guillén, D.-J. Choi, J. I. Pascual, M. M. Ugeda, P. Ordejón, and E. Canadell, Coexistence of elastic modulations in the charge density wave state of 2H-NbSe2, Nano Letters **19**, 3027 (2019).

[5] H. Fukuyama, Pinning in Peierls-Fröhlich state and conductivity, J. Phys. Soc. Jpn. **41**, 513 (1976).

[6] H. Fukuyama and P. A. Lee, Dynamics of the charge-density wave. I. Impurity pinning in a single chain, Phys. Rev. B **17**, 535 (1978).

[7] B. Hildebrand, T. Jaouen, C. Didiot, E. Razzoli, G. Monney, M. L. Mottas, A. Ubaldini, H. Berger, C. Barreteau, H. Beck, D. R. Bowler, and P. Aebi, Short-range phase coherence and origin of the 1T-$TiSe_2$ charge density wave, Phys. Rev. B **93**, 125140 (2016).

[8] A. M. Novello, M. Spera, A. Scarfato, A. Ubaldini, E. Giannini, D. R. Bowler, and C. Renner, Stripe and short range order in the charge density wave of 1T-Cu_xTiSe_2, Phys. Rev. Lett. **118**, 017002 (2017).

[9] U. Chatterjee, J. Zhao, M. Iavarone, R. Di Capua, J. P. Castellan, G. Karapetrov, C. D. Malliakas, M. G. Kanatzidis, H. Claus, J. P. C. Ruff, F. Weber, J. van Wezel, J. C. Campuzano, R. Osborn, M. Randeria, N. Trivedi, M. R. Norman, and S. Rosenkranz, Emergence of coherence in the charge-density wave state of 2H-$NbSe_2$, Nature Communications **6**, 6313 (2015).

[10] W. Jolie, T. Knispel, N. Ehlen, K. Nikonov, C. Busse, A. Grüneis, and T. Michely, Charge density wave phase of VSe_2 revisited, Physical Review B **99**, 115417 (2019).

[11] A. Soumyanarayanan, M. M. Yee, Y. He, J. van Wezel, D. J. Rahn, K. Rossnagel, E. W. Hudson, M. R. Norman, and J. E. Hoffman, Quantum phase transition from triangular to

stripe charge order in $NbSe_2$, Proc. Natl. Acad. Sci. **110**, 1623 (2013).

[12] J. Dai, E. Calleja, J. Alldredge, X. Zhu, L. Li, W. Lu, Y. Sun, T. Wolf, H. Berger, and K. McElroy, Microscopic evidence for strong periodic lattice distortion in two-dimensional charge-density wave systems, Physical Review B **89**, 165140 (2014).

[13] G. Grüner, *Density waves in solids* (Westview Press, 2000).

[14] B. Voigtländer, *Scanning probe microscopy: Atomic force microscopy and scanning tunneling microscopy* (Springer, 2015).